Digital Beam-Forming for Spaceborne Reflector-Based Synthetic Aperture Radar Part I: Basic Imaging Modes

Marwan Younis, *Fellow, IEEE,* Felipe Queiroz de Almeida, Michelangelo Villano, *Senior Member, IEEE,* Sigurd Huber, Gerhard Krieger, *Fellow, IEEE,* Alberto Moreira, *Fellow, IEEE*

***Abstract*—Deployable reflector antennas illuminated by a digital feed array enable spaceborne Synthetic Aperture Radar (SAR) systems capable to image an ultra-wide continuous swath at fine azimuth resolution. This is facilitated by the use of dedicated imaging modes and by multi-dimensional digital beam-forming techniques. This paper is part I of a tutorial trilogy, where focus is put on the required on-board functionality, operational techniques, and the digital beam-forming aspects, for which a rigorous mathematical description is included. To maintain general validity, the functional implementation for the various modes is detailed, thus avoiding restricting the description to a specific realization.**

The reader is assumed to be familiar with the general concept of synthetic aperture radar, and otherwise referred to the literature on the topic. The approach followed in the trilogy is to start with a basic simple imaging concept and then move to more advanced modes, thus successively increasing the complexity; the mathematical description follows the same approach.

***Index Terms*—synthetic aperture radar (SAR), digital-beam forming, reflector-based SAR.**

I. Introduction

SYNTHETIC Aperture Radar (SAR) has been widely used for Earth remote sensing for more than 40 years. SAR is unique in its imaging capability: It provides high-resolution two-dimensional images independent from day light, cloud coverage and weather conditions. A wealth of excellent literature exists on the topic as in [1], [2], [3], [4], [5], [6]. Spaceborne SAR systems have a side-looking imaging geometry and are based on a pulsed radar installed on a platform with a forward movement. The flight direction is denoted as *azimuth* and the line-of-sight as *slant range* direction. The time associated to the propagation of the electromagnetic waves at the speed of light is commonly referred to as *fast* time, whereas the time related to the –much slower– platform movement is the *slow* time. The radar system transmits frequency modulated electromagnetic pulses (commonly referred to as *chirps*) with high power and receives the echoes of the backscattered signal in a sequential way. The swath width of spaceborne systems varies typically from 30 to 400 km. The transmitted pulse interacts with the Earth surface and only a portion of it is backscattered to the receiving antenna. The amplitude and phase of the backscattered signal depends on the physical and electrical properties of the imaged object. Commonly used frequency bands in SAR systems range from P-band (250–500 MHz) to X-band (8–12 GHz), but even frequencies up to Ka-band (26.5–40 GHz) are being considered for future missions. More penetration of the electromagnetic pulses in media will occur for radar systems using longer wavelengths. The simplest radar system provides a 2-D reflectivity map of the imaged area, i.e., targets with high backscattered signal are identified as bright spots in the SAR images and flat smooth surfaces as dark areas.

This paper, part I of the trilogy, is organized as follows: In the following section II, the basic instrument architecture for digital beam-forming SAR is introduced. Focus is put on various elements of a reflector-based multiple channels instrument, capable of utilizing digital beam-forming (DBF) based imaging modes. Next, in section III the basic DBF mode, known as Scan On-REceive (SCORE), is introduced; this includes a functional description, the mathematical beam-forming models, as well as a hardware implementation schematic. Section IV addresses implementation particularities of SCORE, such as the digital weight update rate, and the feed activation matrix. An extension to SCORE using frequency-dependent beam-forming, known as dispersive SCORE, is covered in section V and concludes the basic imaging mode of the trilogy's first part. Throughout the paper, typical values for the various design parameters are given to allow the reader to get a deeper understanding of the topic.

II. Digital Beam-Forming SAR

In the last years a trend towards SAR systems with multiple digital channels has manifested itself. This marks a paradigm change resulting from research activity in the last decades. The main innovative characteristic of forthcoming generations of SAR instruments is the use of multiple elevation and/or azimuth receiver channels equiped with digital beam-forming (DBF) capabilities [7], [8], [9], [10], [11], [12]. Even MIMO (Multiple Input Multiple Output) SAR becomes possible [13], [14], [15], [16] by utilizing multiple transmit channels. The virtue of DBF SAR is that it allows the conception of new systems, which overcome the "fundamental limitation" of conventional SAR [17] by extending the dimensionality of the trade-space [13], [18] enabling a substantial performance improvement [19].

Large unfurlable reflector antennas are not new in spaceborne applications as they were used since the early 1960s

All authors are with the Microwaves and Radar Institute of the German Aerospace Center (DLR), Germany. Marwan Younis and Alberto Moreira are also with the Karlsruhe Institut für Technologie (KIT). Gerhard Krieger is also with the Friedrich-Alexander-Universität Erlangen-Nürnberg (FAU)

[20]. To accommodate reflectors with diameters larger than that of the launcher shroud, typically reflectors with a rigid central part and a deployable mesh rim are used. The virtue of unfurlable reflectors, compared to planar, direct radiating, phased-array antennas of comparable size, is their low mass and compact storage volume during launch [21]. For SAR, reflector antennas have been shown to be especially advantageous when combined with a digital feed array [22], [23], [24]. The feed consists of multiple antenna elements arranged as an $N_{az} \times N_{el}$ array in azimuth and elevation, respectively. Fig. 1 shows one feed column of N_{el} elevation channels, where each feed element is followed by an RF front-end, which may be implemented as a simplified Transmit/Receive Module (TRM). This is followed by a digitizer and the digital processing unit. Such a system allows the use of the digital beam-forming techniques, mentioned above, by utilizing the data samples of the SAR echo signal received by each antenna element of the array.

Digital beam-forming for SAR can be realized with parabolic reflector antenna systems combined with a digital feed array, or planar antenna systems. The configuration in Fig. 1 is representative for either antenna type, however the technique used for the beam pointing is rather different. As will be detailed later, the beam position of a reflector is varied by changing (electronically) the effective position of the active feed element. In planar antennas, the beam pointing is determined by the slope of a linear phase excitation applied over all antenna elements.

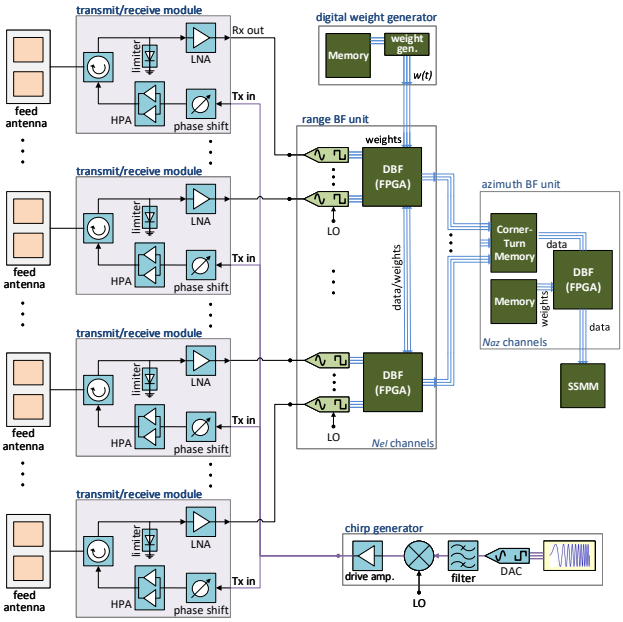

Figure 1: Schematic of digital feed array showing an N_{el} element column (antenna radiators, transmit-receive modules, digitizers) of the feed matrix followed by the digital processing unit in range and azimuth.

In DBF systems, the complexity of the RF hardware is often reduced, while the demand for the on-board digital processing capabilities grows [25], [26]. This is reflected in the instrument concept, where the TRM, cf. Fig. 2, basically consists of a phase shifter in the transmit path followed by an amplifier and a circulator (or switch); while the main part of the receive path is the low noise amplifier (LNA). These are significantly simplified compared to the phased-array TRMs in state-of-the-art SAR. The same is true for the calibration, where a simple cal-tone coupler may be used instead of an elaborate TRM-internal calibration unit [27], [28], [29]. On the other hand, the digital unit must handle and process multiple data streams, as described here in detail.

Parameter Values: Reflector SAR systems are capable of imaging swathes in the order of 300 km to 400 km; the diameter of the reflector antenna is typically >12 m. The feed array consists of $N_{el} \times N_{az}$ antenna elements in elevation (cross-track) and azimuth (along-track), respectively. Typically N_{el} may be as large as 28 to 36, while N_{az} is usually smaller than 4.

The radiation pattern of the feed elements are commonly referred to as *primary* patterns, which illuminate the reflector surface generating the *secondary* patterns. If the main lobe of the primary pattern illuminates an area which is larger or smaller than the reflector area, then the reflector is over- or under-illuminated, respectively. The term *antenna element* should more generally be replaced by *sub-array*, thus taking into account that the feed array may be divided into sub-arrays (cf. Fig. 1), each consisting of several *radiators*. For example, in Fig. 2 a passive feed network combines two patch elements into a sub-array. As the focus is on the digital part it is mostly irrelevant how many radiators constitute a sub-array, thus motivating the lax use of the term antenna element here. In terms of the system performance, however, these are key aspects which have an essential impact on the beam-forming and therefore also on performance such as the ambiguity-to-signal ratio and the cross polarization cancellation [30]. In general, it can be said that, if a sub-array's primary pattern under-illuminates the reflector, then there is a loss in signal-to-noise ratio because the aperture area is not fully utilized. Whereas, on the other hand, a strong over-illumination is an indication that more antenna elements can be combined into a sub-array, thereby reducing the primary beamwidth and by this the spillover loss [31]; this also reduces the number of digital channels.

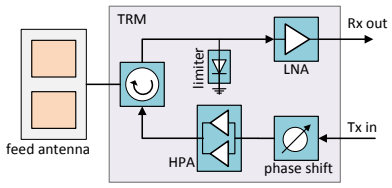

Figure 2: Simplified schematic of Transmit/Receive Module (TRM) connected to the feed antenna; here a sub-array is formed out of two radiators.

III. Basic (Single-Beam) SCORE Imaging Mode

Consider a SAR instrument which successively transmits frequency modulated pulses (chirps) of fixed duration τ_p (cf. Fig. 3) illuminating a wide swath on the ground. The pulses are transmitted at a regular rate, every T_{pri} seconds, commonly known as the Pulse Repetition Interval (PRI).

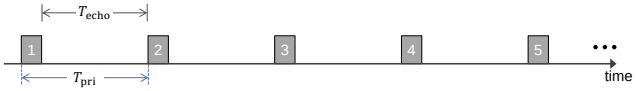

Figure 3: Transmit pulse sequence versus time. The duration of the ground echo return is T_{echo}.

The minimum Pulse Repetition Frequency (PRF) of a SAR system, f_{prf}, is inversely proportional to the size of the antenna, given here by the diameter of the reflector D, and may be approximated by:

$$f_{\text{prf}} = \frac{1}{T_{\text{pri}}} \geq a\frac{2v_{sat}}{D} \tag{1}$$

with T_{pri} the pulse repetition interval; v_{sat} the satellite platform velocity; and a a proportionality constant, which depends on the illumination of the reflector by the feed array[1], the operation mode, and the processed Doppler bandwidth, i.e., azimuth SAR image resolution.

The expression in (1) is derived taking into account a radiation pattern beamwidth which is inversely proportional to the electrical antenna aperture size. The proportionality constant a mainly depends on the reflector illumination (or the amplitude taper in a planar antenna) with values in the range $a \approx 1.22$ to 1.5. Typical values for T_{pri} are then 250 µs to 500 µs, corresponding to a PRF of 2 kHz to 4 kHz. The duty cycle is around 4 % to 10 % of the T_{pri}, resulting in a pulse duration τ_p of a few tens of microseconds.

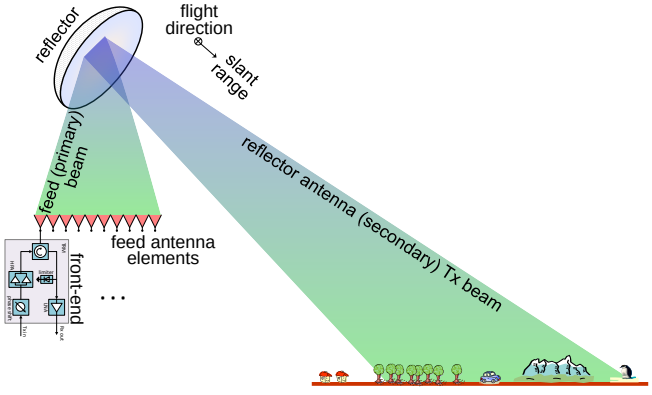

Figure 4: Reflector SCan-On-REceive (SCORE) Tx illumination. All feed array elements are active generating a narrow primary beam which under-illuminates the reflector, thus generating a wide secondary beam which illuminates the complete swath to be imaged.

[1]For example, if multiple azimuth antenna feeds are combined on receive, then the effective illumination area of the reflector is decreased leading to a higher PRF.

On transmit, all $N_{el} \cdot N_{az}$ antenna elements of the feed array are activated with maximum amplitude (uniform amplitude taper); this generates a narrow primary beam, which illuminates a small part of the reflector, i.e., the feed is under-illuminating the reflector, which in turn generates a wide secondary beam to illuminate the complete swath, as shown in Fig. 4. A phase taper is applied to optimize the beam shape, thus requiring phase control on-transmit, typically achieved through appropriate TRM (Transmit/Receive-Module) setting [32].

A. Functional SCORE Description

In 1981 Blyth [33] suggested a basic approach for analog beam-steering using variable phase shifters such that the receive beam of a planar antenna moves over the swath in accordance with the position of the echo. About twenty years later his idea finds a more detailed description and justification in the independent and almost contemporary works by Kare [34], and Suess & Wiesbeck [35]. The former extends the idea to reflector antennas, while the latter –for the first time– presents digital beam-forming techniques in conjunction with a time-varying receive beam-steering in elevation.

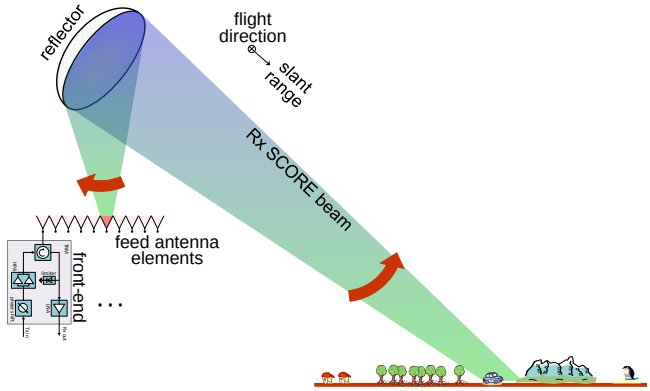

Figure 5: SCORE geometry and operation. A narrow high-gain receive beam is directed towards the echo signal traversing the ground (note, that the antenna beam is shown to converge emphasizing the narrow beamwidth, while the actual beam diverges).

The technique, known as Scan-On-REceive (SCORE), uses multiple channels in elevation to generate a receive beam that follows the SAR signal echo while it traverses the ground [36], [37], see Fig. 5. SCORE allows an effective increase in the receive antenna elevation dimension in order to generate a narrow and high gain beam; this yields a higher signal-to-noise ratio and allows for a better suppression of range ambiguities. The transmit antenna beam still needs to be wide in order to illuminate the complete imaged swath. SCORE is especially attractive if implemented on-board and thus does not result in any substantial increase of the data rate[2]. Viewed in terms of the trade-space, SCORE decouples the imaged swath width from the receiving antenna height [13], [38].

[2]Indeed SCORE can be considered as a loss-less data compression along elevation [27].

Parameter Values: The reference L-band SAR system considered throughout part I of this tutorial operates at 1.24 GHz and has a $D = 15\,\mathrm{m}$ diameter reflector to image a 70 km wide swath.
For an orbit height of $h_{sat} = 700\,\mathrm{km}$ the swath may be positioned between the look (off-nadir) angles $\vartheta_{near} = 28.7°$ and $\vartheta_{far} = 32.7°$, respectively. The receive pattern, scanning the ground, has a beamwidth of 1.1°. On transmit, the reflector is under-illuminated, such that the secondary pattern beamwidth of 4° is sufficient to illuminate the complete swath.

At this point it is sufficient to consider a single column $N_{el} \times 1$ of the receive array; this simplification will be dropped later in Part II and III of the tutorial. The transmitted pulse traverses the ground with the scattered signal causing an echo which is reflected back to the SAR. The duration of the echo signal depends on the swath width and is given by:

$$T_{echo} = \frac{2(R_{far} - R_{near})}{c} + \tau_p \qquad (2)$$

where R_{near} and R_{far} are the near and far limits of the swath, respectively, and τ_p is the duration of the transmit pulse. For a spaceborne SAR the ground pulse extension, which is the area on the ground simultaneously contributing to the echo received at any time instance [39], is smaller than the swath width; its value $\chi_{gr} = \tau_p c/(2\sin\eta_i)$ is in the order of a few kilometres, where η_i is the incidence angle and c the velocity of light. Nevertheless, the pulse extension has major effect on SAR, as detailed in section IV-A and Part II of the tutorial.

Parameter Values: The near and far slant ranges of the reference SAR are $R_{near} = 812\,\mathrm{km}$ and $R_{far} = 852\,\mathrm{km}$, respectively. With a pulse duration of $\tau_p = 29\,\mu\mathrm{s}$ the echo duration, according to (2), becomes $T_{echo} = 0.3\,\mathrm{ms}$.

A particularity of parabolic reflector antennas –when compared to direct radiating planar antennas– is that the energy of the incoming wave is focused to different regions (of the feed array) depending on its angle-of-arrival. A proper reflector/feed design for SCORE operation focuses 90 % of the power on about two feed elements, in which case, for any angle-of-arrival, two to three feed elements are sufficient to collect the main portion of the signal energy. It is noted that the individual feed antenna elements of a feed array designed for SCORE operation are smaller than for conventional single feed design (cf. [34] for a detailed description).

B. Beam-Forming Approach and Mathematical Model

The range-time diagram shown in Fig. 6 is useful for understanding the temporal support of the echo signals received by the feed elements and the relating to the beam-forming. The abscissa and ordinate of the diagram represent time and range, respectively. Each horizontal bar can be thought of as the data array or data samples of one feed element, given by the input signal $\mathbf{s}_n$. The colored strips (patches) –not drawn to scale– show the echo data of the pulse traversing the swath, where, clearly, with increasing time the echo data arrive from near to far range. The signal collected by any feed element is the superposition of all scatterers' echoes within the angular segment covered by the element; it is mathematically represented by a complex sum of a large number of chirp signals.

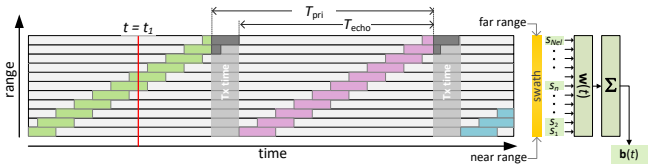

Figure 6: Range-time diagram showing the echo signal data received by the antenna elements and (right side) the digital beam-forming unit.

The echo signal duration for a point target at a fixed range/angle is τ_p. For an extended scene, however, since each feed element covers an angular extent, it "delivers" echo data for $> \tau_p$ seconds [39]. An echo is received every T_{pri} seconds and interrupted by the transmission duration, since the instrument hardware can not transmit and receive simultaneously[3]. During the echo-free times a feed element receives noise and the data array may be filled with zeros. At any time instance $t = t_1$, see vertical line in the figure, two elements are active, i.e., delivering data. The number of active elements may vary depending on the pulse ground extent, the feed/reflector configuration, and the orbit/ground geometry. The beam-former (cf. right side of the figure) applies complex weights on the elements' data which are then combined into one data stream. During the transmit events, marked as vertical gray bars, the reception of all feed elements is blocked; in Fig. 6 this is seen to affect the reception of the far range echo signals. The blockage times are elaborated in Part II and [40].

Thus, in the simplest case, SCORE would be implemented by selecting the antenna element(s) receiving an energy above the noise threshold, sampling the respective signals followed by a digital summation. The simple SCORE is thus a unity beam-former, where each element's signal is either on or off. In practice this procedure would not yield the required SAR performance for two reasons:

1) the finite number of $\leq N_{el}$ switched beams would cause a strong ripple on the received signal power versus elevation angle, and
2) beam shaping cannot be used, which is necessary for example to suppress the range ambiguities or sidelobe cancellation.

Consequently, a more sophisticated approach is used, in which the signal induced on each element is digitized, multiplied by a time-varying digital weight $w_n(t)$, and the result of several channels summed up, as shown in the schematic block diagram of Fig. 7. As these weights are complex numbers (not just 0 or 1 like in the previous simple case), either an I/Q-demodulation or a Hilbert transformation of the real data stream is necessary. The weights can be understood as the

[3]This aspect and its implications is detailed in Part II of the tutorial paper.

beam-forming coefficients which yield the required secondary beam shape pointing to the changing direction-of-arrival of the echo while it traverses the ground.

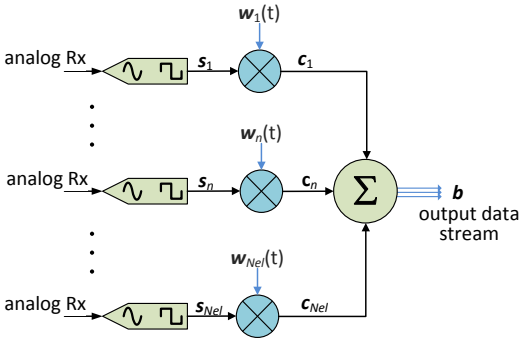

Figure 7: Schematic of digital SCORE implementation: each analog input signal is digitized and the time-discrete complex signal samples (I/Q-demodulation or Hilbert transformation not shown) are then multiplied by a time-varying complex weight. The SCORE beam results after the summation.

The schematic of Fig. 7 shows another important aspect of SCORE: data reduction. SCORE combines N_{el} input data streams into a single output. As such, SCORE can also be understood as a (loss-less) data reduction technique [27]. This $N_{el} : 1$ data reduction is the main reason why SCORE would practically be implemented in real-time on board the SAR instrument despite the additional complexity and cost.

To arrive at the mathematical model, the resulting SCORE beam output sample $b[l]$ is represented as:

$$b[l] = \sum_{n=1}^{N_{el}} s_n[l] \cdot w_n(t) \quad \text{for } l = 0, \ldots, N_{rb} - 1 \tag{3}$$

where l is the sample index; $s_n[l] = s_n(t_l)$ is the sampled signal induced on antenna feed element n, with $t_l = l/f_s$ the discrete sample time for a signal sampled at frequency f_s; and $w_n(t)$ is the complex weight function applied on the signal of channel n. Separate notations are used here to indicate the different time dependencies: the sampled signal changing on a sample-to-sample basis, and the weights which change more slowly than the signal sampling. The number of samples N_{rb} is given by:

$$N_{rb} = T_{echo} \cdot f_s \tag{4}$$

Throughout this paper complex sampling will be assumed; in this case Nyquist sampling requires the sampling rate f_s to be higher than the signal (chirp) bandwidth B_w. For example, in case of the aforementioned I/Q-demodulation, each of the I and Q channels would be sampled at a rate f_s resulting in a data stream of one complex number every $1/f_s$ seconds. As such the N_{rb} is the number of *complex* signal samples.

Parameter Values: For the reference SAR system, which images a swath width of 70 km, the echo duration T_{echo} is $\approx$ 0.3 ms. With a sampling rate of $f_s = 85$ MHz this gives $N_{rb} = 25\,500$ (complex-valued) samples per channel per range line.

A graphical representation useful for understanding the beam data is shown in Fig. 8 and referred to as range-azimuth diagram. It basically shows the signals (data streams) after the beam-forming process, and, as such, is an extension of the range-time diagram shown earlier in Fig. 6. Each column of N_{rb} (complex-valued) samples represents the beam echo data of the full swath for one transmitted pulse – also known as range line. Successive range lines represent the echo data of consecutive Tx pulses at different azimuth positions of the platform. In the figure two range lines have been filled with data, while the echo data of the third pulse has not been fully processed/received.

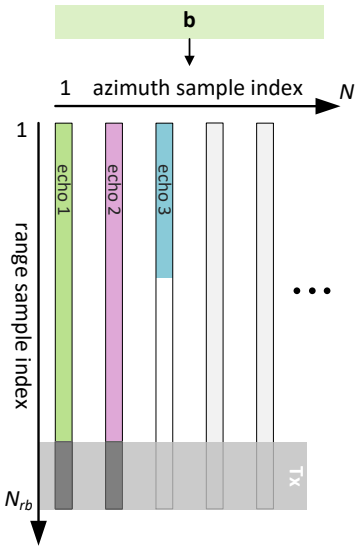

Figure 8: Range-azimuth data diagram showing the data streams after combining, i.e., beam-forming, the signals of the individual elements.

Adopting matrix notation, the sequence $s_n[l]$ of input samples of channel n is written as a column vector:

$$\mathbf{s}_n = \left[s_n[0], s_n[1], \ldots, s_n[N_{rb} - 1]\right]^T \tag{5}$$

where N_{rb}, introduced earlier, represents the total number of time samples of one range line of duration T_{echo}, which is equal to the dimension of the vector (number of elements). The $N_{rb} \times N_{el}$ signal matrix of all elevation channels becomes:

$$\mathbf{S} = [\mathbf{s}_1, \mathbf{s}_2, \ldots, \mathbf{s}_{N_{el}}] \tag{6}$$

Similarly, the N_{rb}-element SCORE output beam vector is defined as:

$$\mathbf{b} = \left[b[0], b[1], \ldots, b[N_{rb} - 1]\right]^T \tag{7}$$

Then, the vector equation corresponding to (3) becomes[4]

$$\mathbf{b} = \mathbf{S}\mathbf{w}(t) \tag{8}$$

with the N_{el}-element weight vector:

$$\mathbf{w}(t) = [w_1(t), w_2(t), \ldots, w_{N_{el}}(t)]^T \tag{9}$$

[4]The confusion that maybe caused by (8) indicating changing weights within a matrix multiplication are addressed and resolved in section IV-B.

C. Polarization

Polarimetric SAR techniques were developed in the 80s and 90s and are nowadays considered established, and widely used for an improved physical parameter retrieval in imaging radar [41], [42].

Dual-pol capability (single transmit polarization and two orthogonal receive polarizations) requires a replication of the same functionality for each polarization channel. Imaging in fully polarimetric mode (quad-pol) in turn requires transmitting a second orthogonal polarization. In conventional SAR, the two transmit polarizations are operated in time multiplex; this requires changing the SAR operation parameters, such as increasing the PRF, which has an impact on the SAR performance. Further, the antenna polarization purity, i.e., the magnitude of the cross-polar component, becomes relevant. Reflector antennas with small focal-length-to-diameter ratios suffer from an intrinsic high cross-polar component; this can be mitigated through special feed array designs [43], [44]. Dedicated SAR technques can be used to enable polarimetric SAR as discussed for example in [45], [46].

The following discussion will assume a single-polarized instrument and thus does not explicitly deal with the polarization topic. This approach is still considered to be general, as adding polarimetric capability basically means duplicating the receive hardware and beam-forming capabilities.

It is straightforward to generalize to N_{pol}^{Tx} transmitted polarizations and N_{pol}^{Rx} received polarizations, amounting to a total of $N_{pol} = N_{pol}^{Tx} \cdot N_{pol}^{Rx}$ polarizations (e.g. 4 for a fully polarimetric system). As such we rely on the reader's common sense to extend the explanations to the dual-pol and quad-pol cases.

IV. Implementation Aspects

In the following, consideration is given to the update rate of the time-varying DBF weights and their correct mathematical matrix representation. Further, the issue of the active channels is addressed.

A. Weight Update Rate

The weights are updated at a rate slower than the signal sampling, where the minimum update rate should be chosen to ensure a smooth transition from one discrete beam position to the other and to avoid losses caused by the pulse moving out of the beam. The update rate depends on many parameters including, for example, the reflector size, instrument PRF, pulse duty cycle as well as the specific digital beam-forming algorithm and by this the values of the weights themselves. This is why the exact update rate is usually determined through simulations, which include all relevant parameters. In the following a simple criteria is detailed, which can be applied to arrive at reasonable approximations for the weight number and update rate. The reader interested in more details including other possible criteria is referred to [47], [48], which elaborate on this topic and present simulation examples and performance values.

The beamwidth Φ of an antenna is defined by the half-power (i.e., 3-dB) angular extent of the radiation pattern's main-lobe. For a uniform taper it is proportional to the ratio of wavelength to antenna aperture size. The beamwidth of the secondary receive (SCORE) pattern depends on the reflector illumination by the primary feed pattern; for the cases of interest here, it will be assumed independent of the scan angle and may be approximated by $\Phi = a\lambda/D$, where D is the reflector diameter and $a \approx 1.22$ to 1.5, the proportionality constant, cf. the expression in (1). A second parameter of interest is the angular pulse extent, which is a measure of the instantaneous angular segment covered by the transmit pulse of duration τ_p. In [39] an expression for the angular pulse extent as a function of the look (or off-nadir) angle ϑ is derived and given by:

$$\chi_\vartheta(\vartheta) = \frac{\tau_p c}{2r_O\left(\frac{r_O\cos\vartheta}{\sqrt{r_E^2-(r_O\sin\vartheta)^2}}-1\right)\sin\vartheta} \tag{10}$$

where r_E and $r_O = r_E + h_{sat}$ are the Earth and orbit radii, respectively. Evaluating the above expression shows that the pulse extent decreases with increasing look angle. Fig. 9 (top) shows the antenna pattern and pulse extent versus look angle for the case that the antenna pattern is steered to the pulse center.

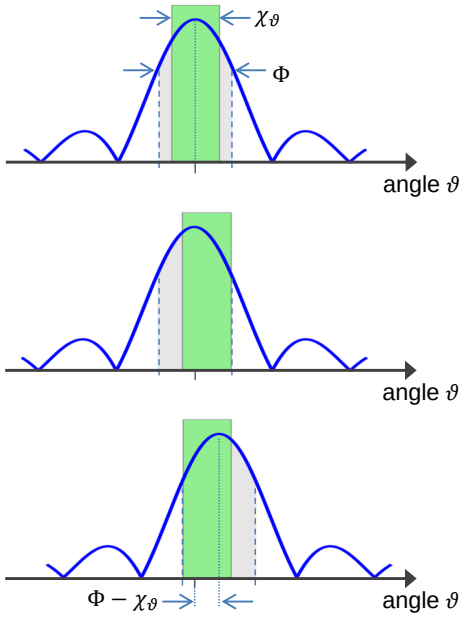

Figure 9: Antenna receive radiation pattern and pulse angular extent versus elevation angle (top); the pulse moves over the ground and when it reaches the half-power point of the radiation pattern (middle) the weights are updated generating a new SCORE beam shifted by $\Phi - \chi_\vartheta$ (bottom).

Now, a reasonable requirement is that the pulse edge is allowed to just touch the half power point of the secondary radiation pattern. Thus, whenever the pulse has moved far enough out of the pattern maximum, cf. Fig. 9 (middle), the weights are updated, thus effectively moving the pattern ahead of the pulse as shown in Fig. 9 (bottom). As a result the pulse edges are kept within the beamwidth of the radiation pattern at all times.

The SCORE beam is thus steered from one fixed direction to the next, emulating a smooth movement. With the condition

above, and assuming that the beamwidth is larger than the angular pulse extent $\Phi > \chi_\vartheta$, the steering angle step is:

$$\Phi - \chi_\vartheta(\vartheta) = \frac{a\lambda}{D} - \chi_\vartheta(\vartheta) \tag{11}$$

To determine the number of SCORE beams, take the swath width $(\vartheta_{far} - \vartheta_{near})$ in angular units[5] and divide by the step size to yield the total number of steps:

$$M_w = \frac{\vartheta_{far} - \vartheta_{near}}{\frac{a\lambda}{D} - \chi_\vartheta(\vartheta_{near})} \tag{12}$$

where the step size is fixed to its minimum value over the swath, i.e., taking $\chi_\vartheta(\vartheta_{near})$, in order to arrive at an upper limit for M_w.

Finally, the maximum update rate of the weights is given by the inverse of the time the beam coefficients remain fixed:

$$\begin{aligned}\Delta T_w &= \frac{1}{f_w} = \frac{T_{echo}}{M_w} \\ &= \frac{T_{echo}}{\vartheta_{far} - \vartheta_{near}} \left(\frac{a\lambda}{D} - \chi_\vartheta(\vartheta_{near}) \right)\end{aligned} \tag{13}$$

Parameter Values: Consider the reference SAR system with a $D = 15\,\mathrm{m}$ reflector diameter. The swath limits are set such that $\vartheta_{far} - \vartheta_{near} = 4.0°$. For a pulse duration of $\tau_p = 29\,\mu\mathrm{s}$ the angular pulse extent $\chi_\vartheta(\vartheta)$ varies from $0.5°$ to $0.4°$, while the pattern beamwidth is $1.1°$. Then $M_w = 6.7$ distinct weights are applied, which are updated at a rate of $f_w \approx 22\,\mathrm{kHz}$.

It should be emphasized that the above values are obtained based on one possible criteria for the beam transition; the aim was to show that how a simple models may be formed to estimate the number of beam transitions. Taking into account aspects, such as ground topography, antenna pointing errors, impact of phase jumps on interferometric applications, or the pattern calibration, will lead to other criteria and may result in rather different values.

B. Clarification to the Correct Usage of Matrix Notation

The weight vector $\mathbf{w}(t)$ is explicitly written as a function of time to allow for a simpler mathematical representation and also indicating that the weights change more slowly than the signal sampling. However, a straightforward application of matrix multiplication in (8) is ambiguous and would probably not yield the right result. To explain this, considering an arbitrary column of the matrix $\mathbf{S}$; the direct application of (8) would cause all N_{rb}-elements of $\mathbf{s}_n$ to be multiplied by the same weight $w_n(t)$; which clearly neglects that the weights change with the time sample index l of $s_n[l]$.

A correct matrix notation is stated here for completeness, and as justification to later maintain the simpler time-function representation, which is believed to give a better insight into the beam-forming process.

[5]The angular swath extent is the minimum look angle subtracted from the maximum look angle; in slant range, this corresponds to $(R_{far} - R_{near})$ and the temporal swath extent is T_{echo}.

To arrive at the correct matrix equation corresponding to (8) the signal matrix $\mathbf{S}$ is rewritten as an $N_{rb} \times (N_{el} \cdot M_w)$ block (or partitioned) matrix $\mathbf{S}_\mathrm{p}$. A block matrix can be interpreted as being broken into sections called blocks or sub-matrices; here all off-diagonal blocks are zero matrices. The signal matrix is thus given by:

$$\mathbf{S}_\mathrm{p} = \begin{bmatrix} \mathbf{S}_{\mathrm{p}1} & 0 & \cdots & \cdots & 0 \\ 0 & \mathbf{S}_{\mathrm{p}2} & 0 & \ddots & \vdots \\ \vdots & \ddots & \mathbf{S}_{\mathrm{p}3} & \ddots & \vdots \\ \vdots & \ddots & \ddots & \mathbf{S}_{\mathrm{p}4} & 0 \\ 0 & \cdots & \cdots & 0 & \mathbf{S}_{\mathrm{p}M_w} \end{bmatrix} \tag{14}$$

where each $\mathbf{S}_{\mathrm{p}i}$ for $i = 1, \cdots, M_w$ is an $m_i \times N_{el}$ sub-matrix, such that $\sum_{i=1}^{M_w} m_i = N_{rb}$. The elements of $\mathbf{S}_{\mathrm{p}i}$ are then given by m_i complex signal samples of all channels. Note that the number of rows and by this the size of the sub-matrices may change over range, taking the typical SAR geometry and antenna beamwidth into account; this is because the slope of the angle-to-range mapping function and the antenna-beamwidth change over off-nadir angle.

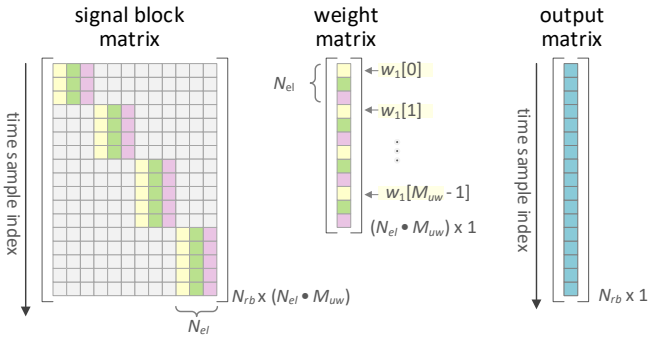

Figure 10: Schematic of matrix multiplication.

The structure of the block matrix is shown in the left of Fig. 10 for the case of $N_{el} = 3$ elevation channels and $M_w = 4$ unique sets of weights. Each row includes N_{el} nonzero elements which are the signal samples for a single time instance l, while all other elements are zero.

Consider the number M_w of unique weights within the echo window time, which is smaller than the number of range bins $M_w \ll N_{rb}$, because the weights change slower than the signal samples. The time-discrete weights of channel n are now written as $w_n[0], w_n[1], \ldots, w_n[M_w - 1]$, where, in general $w_n[i] \neq w_n[j]\ \forall\ i \neq j$. The $M_w \cdot N_{el}$ element "unique" weight vector $\mathbf{w}_{uw}$ is defined as:

$$\begin{aligned}\mathbf{w}_{uw} = \big[&w_1[0], \cdots, w_{N_{el}}[0], w_1[1], \cdots, w_{N_{el}}[1], \cdots, \\ &w_1[M_w - 1], \cdots, w_{N_{el}}[M_w - 1]\big]^T\end{aligned} \tag{15}$$

which is the ordered set of all weights over time as shown in the center of Fig. 10.

With the above, the output vector $\mathbf{b}$ is given by:

$$\mathbf{b} = \mathbf{S}_\mathrm{p} \mathbf{w}_{uw} \tag{16}$$

which is the equivalent to (8) in correct matrix notation. It is worth to remember that the two steps necessary to arrive at

this notation are: writing the signal matrix $\mathbf{S}$ as a block matrix $\mathbf{S}_{\mathrm{p}}$, and inserting the set of complex weights into a new weight vector $\mathbf{w}_{uw}$.

C. Activation Matrix

The mathematical model introduced in the previous section applies to both planar and reflector antenna systems [21], as the weights are applied to all N_{el} elevation channels. In the case of a reflector antenna, the echo signal energy is focused on a small number of feed elements, such that N_{act} of N_{el} feed elements are summed[6]. The change of the echo's angle-of-arrival causes the signal's energy to be focused on varying feed array elements as shown in Fig. 11 for three angles.

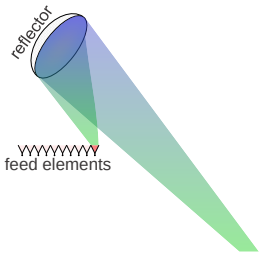

(a) SCORE beam 1 (near range)

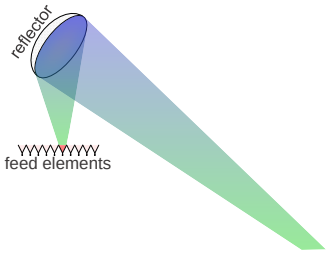

(b) SCORE beam 2 (mid range)

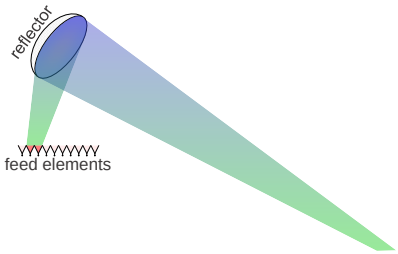

(c) SCORE beam 3 (far range)

Figure 11: A reflector with a digital feed array focuses the power on different feed elements depending on the direction-of-arrival of the signal.

The set of feed array elements $\mathcal{N}_{act}$ on which the echo signal is induced at any instance of time are called *active*. The set of active elements and its size, i.e., total number of active elements are:

$$\mathcal{N}_{act}(t) = \{n_0(t), \ldots, n_1(t)\} \tag{17}$$

[6]Here, N_{act} feeds have approximately the radiation area of a single non-SCORE feed, and $N_{el}/N_{act}-1$ is the number of beam widths of scan needed [34].

where $1 \leq n_0 \leq n_1 \leq N_{el}$, and

$$N_{act} = |\mathcal{N}_{act}(t)| = n_1(t) - n_0(t) + 1, \tag{18}$$

respectively, where the latter is assumed to remain constant, i.e., N_{act} is independent of time[7]. However, the elements which are active change while the echo signal is received from different directions. This is accounted for by including the time dependency in $\mathcal{N}_{act}(t), n_0(t)$, and $n_1(t)$. With reference to Fig. 6, the activation matrix can be understood as a mask, placed on the data of the feed elements to select only the samples of relevant signal energy.

From a theoretical perspective it is always beneficial to extend the beam-forming to the maximum number of elements which can for example be used for sidelobe reduction and ambiguity suppression. However, the weight of the non-active elements is very small and their utilization requires knowledge of their complex-valued secondary patterns. In the cases where the accuracy of the antenna pattern knowledge is limited, additional elements might only contribute as noise which makes them useless for reflector beam-forming. Part II of the tutorial elaborates on the proper feed element selection approach and provides simulated examples on the effect on the beam-forming performance.

Thus, from a beam-forming perspective, it is perfectly valid to set the weights of noisy data streams to zero, thus $w_n(t) = 0 \ \forall n \notin \mathcal{N}_{act}(t)$ avoiding noise amplification. From a hardware architecture point of view, however, it does not make sense to waste processing resources by multiplying inactive channels by zero weights. An "economical" design would take this aspect into account by reducing the number of multiplications, as all but N_{act} multiplications are considered unnecessary. With reference to Fig. 7 this would mean limiting the summation to a (changing) set of active elements, such that the output data vector is given by:

$$\mathbf{b} = \sum_{n \in \mathcal{N}_{act}(t)} \mathbf{s}_n w_n(t) = \sum_{n=n_0(t)}^{n_1(t)} \mathbf{s}_n w_n(t) \tag{19}$$

On the other hand, reducing the number of multipliers may, however, not be worthwhile as it requires the implementation of an elaborated data routing procedure.

Parameter Values: Usually the echo signal of each antenna element is digitized, i.e., no combination of the RF signals is applied. The number of active elements, N_{act}, can be as small as 2 to 4 in basic (single) SCORE. Applying beam-forming for sidelobe suppression requires activating elements outside the signal focus in which case N_{act} may be as large as 8 to 14.

Mathematically the selection of the set of active antenna elements $\mathcal{N}_{act}$ can be represented through an $N_{el} \times N_{act}$ binary activation matrix $\mathbf{A}_{act} = [a_{i,j}; i = 1, 2, \ldots, N_{el}, j =$

[7]Due to the geometry a constant 1 km of ground range is mapped to a decreasing angular segment from near to far range. Further, reflector antennas exhibit a defocusing effect for large angle-of-arrival deviations w.r.t. boresight. Both effects cause the number of active channel to change. Strictly speaking, this effect should be considered, but it is ignored here for the sake of simplicity.

$1, 2, \ldots, N_{act}]$, where $N_{act} \leq N_{el}$. The activation matrix is a Toeplitz matrix $a_{i,j} = a_{i+1,j+1} = a_{i-j}$, the first column of which is an N_{el} element unit vector $\mathbf{e}_i$, i.e., a vector with zeros in all of its entries, except the i-th entry which is set to 1. The activation matrix thus "selects" antenna elements $n = n_0, n_0 + 1 \cdots, n_0 + N_{act} - 1$; as the set of selected elements $\mathcal{N}_{act}(t)$ change with time, the activation matrix itself also becomes a function of time. With this:

$$\mathbf{b} = \big(\mathbf{S}\mathbf{A}_{act}(t)\big)\acute{\mathbf{w}} = \acute{\mathbf{S}}\acute{\mathbf{w}} \tag{20}$$

where the term in parentheses is an $N_{rb} \times N_{act}$ matrix and the modified N_{act}-element weight vector $\acute{\mathbf{w}}$ now includes only nonzero entries.

D. Hardware Realization versus Mathematical Description

In the following, the difference between the mathematical expressions and the computations required to implement these expressions by the hardware are considered.

The expressions in (8) and (20) suggest that the SCORE output data are computed in a single-shot matrix-vector multiplication. The underlying hardware implementation would rather generate individual outputs for each channel $c_n[l] = s_n[l] \cdot w_n(t)$ for $l = 0, 1, \ldots, N_{rb} - 1$, which, when written in vector notation becomes:

$$\mathbf{c}_n = \mathbf{s}_n w_n(t) \tag{21}$$

where $\mathbf{c}_n$ is the N_{rb}-element vector of channel n, and then sum up the individual channel data streams (cf. Fig. 7) to generate the output beam:

$$\mathbf{b} = \sum_{n=n_0}^{n_1} \mathbf{c}_n = \sum_{\mathcal{N}_{act}} \mathbf{c}_n \tag{22}$$

These operations are carried out on a sample-by-sample basis at a rate of f_s: One element of each $\mathbf{c}_n$ vector is computed every $1/f_s$ seconds, requiring $4N_{act}$ real-valued multiplications and $2N_{act}$ real-valued additions (both $s_n[l]$ and $w_n(t)$ are complex numbers); at the same time N_{act} complex samples are added to yield one element (sample) of the output vector $\mathbf{b}$, which requires $2(N_{act} - 1)$ real additions.

Note, again, the issue of the matrix notation in (21), which was resolved in section IV-B. Similar to before, a correct notation requires rewriting the signal vector $\mathbf{s}_n$ of channel n as a block matrix $\mathbf{S}_{np}$ and multiplying by a complex weights vector $\big[w_n[0], w_n[1], \cdots, w_n[M_w - 1]\big]^T$ of the that channel.

V. Dispersive SCORE

An effect which should be considered when applying the weights is the pulse extent mentioned before. For large reflector antennas, the secondary beamwidth in elevation may be smaller than the angular pulse extent. This causes the following effects [39]: the pulse extension loss, a radiometric bias, and an amplitude taper on the spectrum of the return signal; the latter results in worsening of the range resolution. These unwanted effects increase when considering ground topography. Frequency-dependent beam-forming can be used to mitigate the above mentioned effects, as detailed next.

Spaceborne SAR systems transmit linearly frequency modulated pulses – known as chirps. As a consequence of the pulse extent, the frequency scattered by an arbitrary ground point at a specific time instance depends on its position within the pulse; this is indicated by the colored point scatterers in Fig. 12a. Since the illuminated scene consists of many such point scatterers (extended targets), the instantaneous return signal is no longer a chirp, but instead it contains all transmitted frequencies.

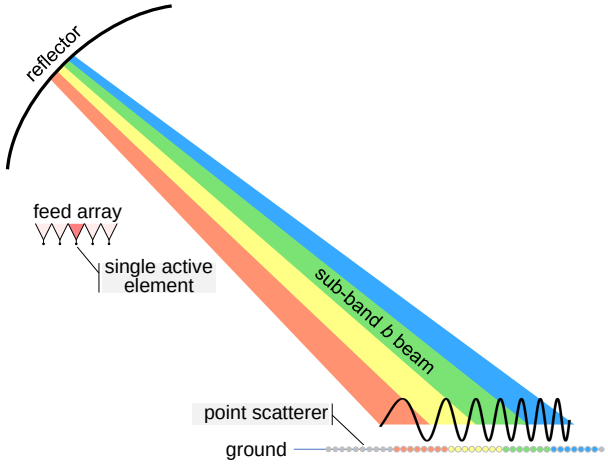

(a) chirp signal traversing the ground and dispersive SCORE beams

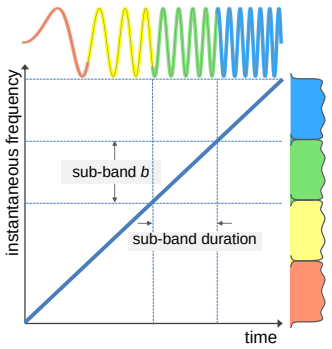

(b) time frequency diagram of transmitted chirp signal

Figure 12: Dispersive SCORE divides the signal spectrum into sub-bands and applies a different weight to each frequency band thus generating a distinct set of frequency-dependent beams.

Nevertheless, each frequency within the return signal's spectrum corresponds to a specific angle-of-arrival. A narrow frequency filter applied on the spectrum of the return signal is also a spatial (and angular) filter suppressing the contribution from all scatterers outside the selected frequency band (in a way equivalent to selecting only the point scatterers of a single color in Fig. 12a), thus effectively reducing the pulse extent and by this the pulse duration. This correspondence between spectrum and angle manifests itself because of the special time-frequency relation of the transmitted pulse (chirp) shown in Fig. 12b

A bank of (digital) bandpass filters (BPF) partitioning the return signal's frequency spectrum, of bandwdith B_w, into

sub-bands (frequency domain) will subdivide the signal into short pulses (time domain). Now a dedicated set of SCORE weights can be applied to each sub-band for optimum beam steering, cf. Fig. 12. The technique of generating frequency (i.e., wavelength) dependent beams is known as *dispersive* SCORE, which is addressed for example in [49]. The effective pulse duration and bandwidth for each sub-band are reduced by a factor equal to the number of sub-bands; for N_{sb} sub-bands this becomes τ_p/N_{sb} and B_w/N_{sb}, respectively.

The inherent wavelength dependency of the reflector secondary patterns motivate the use of dispersive SCORE, even if the pulse extension loss itself is not severe. Partitioning the bandwidth into sub-bands allows compensating this effect and is shown to improve the ambiguity suppression significantly. Conversely, ignoring the frequency dependency might severely impact the performance.

It should be noted that the approach detailed here would fail, if, for example an OFDM (Orthogonal Frequency-Division Multiplexing) signal is transmitted, since there the one-to-one correspondence between frequency, time and angle-of-arrival is lost. Frequency-dependent beam-forming could still be applied, but it would fail in sub-dividing the pulse into shorter time intervals and by this not provide the required performance improvement.

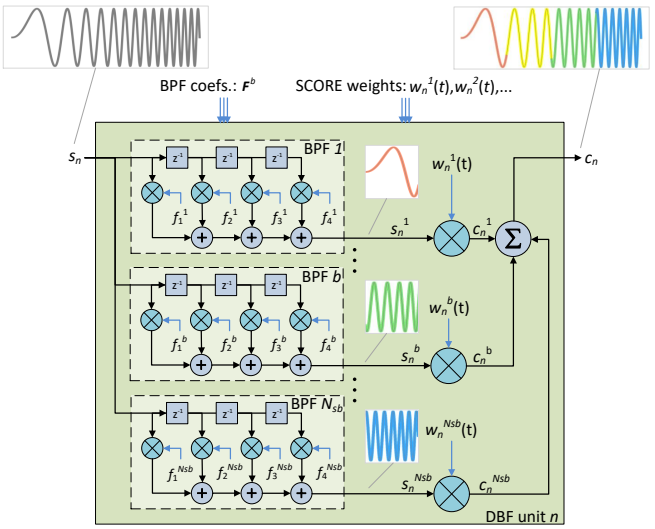

Figure 13: Schematic of filter bank with N_{sb} bandpass filters (BPF) each implemented through an N_{tap}-FIR filter. The time-varying weights are applied to each sub-band generating dispersive SCORE beams. Note that the FIR filter is shown for 4 taps/coefficients, in general a larger number of taps is used.

A. Hardware Realization: Option I

The hardware implementation of the bandpass filters can be achieved using a Finite Impulse Response (FIR) filter bank as shown in Fig. 13. The input data $\mathbf{s}_n$ of each channel are filtered by N_{sb} BPFs each implemented as an N_{tap} FIR filter; the output data stream $\mathbf{s}_n^b$ of each BPF is then multiplied by the time-varying complex weight $w_n^b(t)$. Both the input and output data streams $\mathbf{s}_n$ and $\mathbf{c}_n$ are generated at a rate of f_s samples per second. The FIR filter bank of Fig. 13 is applied to each digital channel, i.e., each multiplier in Fig. 7 is replaced by a filter bank. As shown later, this configuration can, however, be simplified.

In matrix notation, the fixed N_{tap} coefficients of the FIR filter for each sub-band are used to generate an $N_{rb} \times N_{rb}$ square Toeplitz matrix $\mathbf{F}^b$ representing the filters' impulse response functions. The superscript ^{b} will be used to indicate the BPF sub-band $b \in 1, 2, \cdots N_{sb}$, where N_{sb} is the total number of sub-bands or equivalently bandpass filters. The N_{rb}-element signal vector of sub-band b and channel n is obtained through:

$$\mathbf{s}_n^b = \mathbf{F}^b \mathbf{s}_n \tag{23}$$

which is then multiplied by the time-varying SCORE weight $w_n^b(t)$ for each sub-band and channel. After applying the weighs, the sub-bands are combined into one data stream for each channel, given by

$$\mathbf{c}_n = \sum_{b=1}^{N_{sb}} \mathbf{c}_n^b = \sum_{b=1}^{N_{sb}} \mathbf{s}_n^b w_n^b(t) = \sum_{b=1}^{N_{sb}} \mathbf{F}^b \mathbf{s}_n w_n^b(t) \tag{24}$$

where $\mathbf{c}_n$, introduced earlier, represents the N_{rb}-element output of channel n, further, it is emphasized that $\mathbf{F}^b$ is fixed, i.e., here the FIR filters are independent of the channel n and time invariant, whereas the weights $w_n^b(t)$ depend on the channel number, the sub-band, and time[8].

Parameter Values: Typically a small number $N_{sb} \leq 4$ of sub-bands is sufficient to achieve a good performance. A suitable FIR filter length would be in the order of $N_{tap} \leq 10$ taps. Assuming a sampling frequency of $f_s = 85\,\text{MHz}$ the number of complex multiplications per second for *one* channel amounts to: $N_{sb} \cdot N_{tap} \cdot f_s \approx 3400 \times 10^6$ for the fixed weight, plus $N_{sb} \cdot f_s \approx 340 \times 10^6$ for the varying weight, respectively.

Note that an FIR filter with such a small number of taps would not be sufficient to provide a high rejection of adjacent sub-bands. This, however, is not necessary for the dispersive beam-forming as detailed in [49, section 5.2.1], which also provides an analysis of the resulting performance.

B. All-Pass Characteristic

The frequency transfer function of the FIR-BPF filters is non-ideal. This is to say, the signal spectrum $C_n(f) = \mathcal{F}\{c_n(t)\}$ at the output of the BPF bank will be different from its input spectrum $S_n(f) = \mathcal{F}\{s_n(t)\}$, for any channel n. Any modification of the spectrum results in loss of range resolution and/or noise amplification. The mitigation of this unwanted effect is detailed in [49].

It is possible to formulate a condition on the frequency BPF bank such that the spectrum is not modified: with unity weights, the filter bank should not change the signal such that

[8]The time dependency/function means, that different rows of the signal vector $\mathbf{s}_n$ are multiplied by different weights; a strict mathematical formulation, as given in section IV-B, is obviated in favor of a simpler representation.

the output becomes equal to the input. In matrix notation this writes:

$$\mathbf{c}_n = \sum_{b=1}^{N_{sb}} \mathbf{F}^b \mathbf{s}_n \stackrel{!}{=} \mathbf{s}_n \quad \text{for} \quad w_n^b(t) \equiv 1 \tag{25}$$

The above condition requires the combined FIR BPF bank to have an all-pass characteristic, which, however, is not the case for any individual BPF $\mathbf{F}^b$.

C. Weight Update Rate

Dispersive SCORE is typically applied when the angular pulse extent $\chi_\vartheta(\vartheta)$ becomes larger than the secondary antenna beamwidth Φ. Direct application of (12) and (13) would result in erroneous (negative) results, because $\chi_\vartheta(\vartheta) > \Phi$ violating the assumptions in section IV-A.

To arrive at the correct results, the aforementioned effective shortening of the pulse duration in dispersive beam-forming needs to be taken into account, which results in a reduction of the angular pulse extent by a factor of N_{sub}. Inserting into (12) and (13) results in the following expressions:

$$M_w^b = \frac{\vartheta_{far} - \vartheta_{near}}{\frac{a\lambda}{D} - \frac{\chi_\vartheta(\vartheta_{near})}{N_{sub}}} \tag{26}$$

and

$$\Delta T_w^b = \frac{1}{f_w^b} = \frac{T_{echo}}{\vartheta_{far} - \vartheta_{near}} \left(\frac{a\lambda}{D} - \frac{\chi_\vartheta(\vartheta_{near})}{N_{sub}} \right) \tag{27}$$

D. Hardware Realization: Option II

A simpler hardware implementation is motivated by noticing that the input signal vector is the same for all sub-bands, which allows taking $\mathbf{s}_n$ out of the summation in (24), thus yielding:

$$\mathbf{c}_n = \left(\sum_{b=1}^{N_{sb}} \mathbf{F}^b w_n^b(t) \right) \mathbf{s}_n = \left(\sum_{b=1}^{N_{sb}} \mathbf{G}_n^b(t) \right) \mathbf{s}_n = \mathbf{G}_n(t)\mathbf{s}_n \tag{28}$$

which merges the BPF Toeplitz matrices and the time-varying weights into a single band $N_{rb} \times N_{rb}$ matrix

$$\begin{aligned} \mathbf{G}_n(t) &= \mathbf{G}_n^1(t) + \cdots + \mathbf{G}_n^{N_{sb}}(t) \\ &= \mathbf{F}^1 w_n^1(t) + \cdots + \mathbf{F}^{N_{sb}} w_n^{N_{sb}}(t) \end{aligned} \tag{29}$$

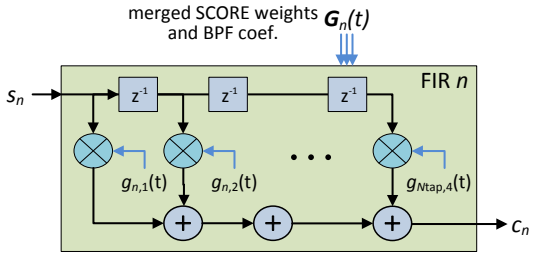

Figure 14: A simplified realization compacting the BPF bank by combining it with the multiplication by the time-varying weights for dispersive beam-forming.

The hardware implementation of (28) is shown in Fig. 14 (replacing the filter bank of Fig. 13). Here the FIR and SCORE weights are merged thus requiring less resources in terms of multiplications and additions. It should be kept in mind, however, that now the weight matrix $\mathbf{G}_n(t)$ changes with time, which means that more resources are needed to compute or store the weights.

Parameter Values: Using the same example as before, i.e., $N_{sb} = 4$, $N_{tap} = 10$ and $f_s = 85\,\text{MHz}$, the number reduces to $N_{tap} \cdot f_s \approx 850 \times 10^6$ complex varying-weight multiplications per second per channel. In this case the weights are either pre-computed and stored in memory, or computed on-the-fly requiring $N_{sb} \cdot N_{tap} \cdot f_w^b$ complex multiplications per second.

One point to mention here is that dispersive beam-forming has the capability to apply a bandpass filter on the return signal, and by this reduce the amount of data. This makes sense if the ratio of sampling frequency to chirp bandwidth $f_s/B_w \gtrsim 1.25$, where 1.25 is the nominal oversampling value (for complex sampling $f_s = B_w$ is the minimum sampling rate to avoid aliasing). A higher oversampling may occur in specific operational modes, if the transmitted chirp bandwidth is reduced, but the ADC sampling frequency fixed to the nominal value. In this case the dispersive beam-forming can be implemented to filter the signal data, improving the signal-to-noise ratio [50], and, at the same time, reducing the data rate. The topic is not further elaborated here, as the implementation is straightforward.

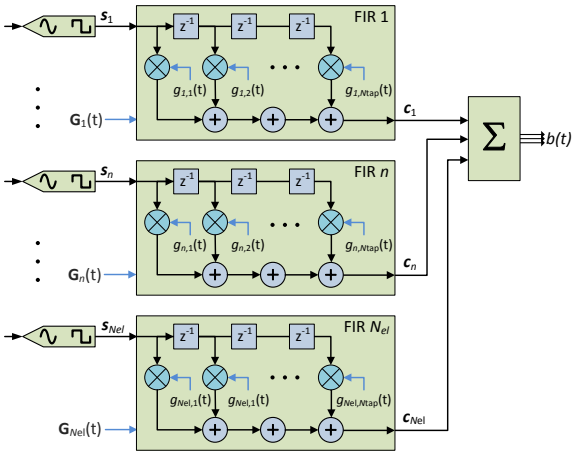

Figure 15: Schematic of dispersive SCORE implementation, where each FIR filter merges the SCORE and BPF coefficients and is applied to the input date stream. The dispersive SCORE beams results after the summation.

To summarize, dispersive SCORE is a frequency-dependent beam-forming. The instantaneous-frequency-to-time mapping particular to the transmitted frequency modulated (chirp) waveform and the side-looking SAR geometry result in one-to-one time, frequency, and angle-of-arrival mapping, utilized here to overcome the disadvantages of monochromatic SCORE

beam-forming.

Dispersive beam-forming requires passing the signal of each channel through an FIR filter bank, which allows tuning the beam-forming coefficients, applied to the filters' outputs, depending on the frequency band. It was further shown that the filter bank may be replaced by an equivalent single FIR filter with time-varying coefficients[9]. A complete multi-channel dispersive beam-forming network is shown in Fig. 15; this is the dispersive version of the monochromatic beam-forming network of Fig. 7.

VI. Concluding Remarks

This paper provides a tutorial-type introduction to the basic DBF imaging modes of SAR utilizing a reflector antenna in conjunction with a digital feed array. This paper has shown the instrument architecture of a multi-channel SAR system and how it may be utilized for digital beam-forming. A property of parabolic reflector antennas is to concentrate (focus) the energy of the incoming electromagnetic wave onto a small area; a change in the direction-of-arrival will shift the focus point. Properly positioning the feed array will cause the incoming echo signal to be focused on different feed elements. Utilizing a multi-channel feed array allows for digital beam-forming, different from that of a planar antenna. SCan-On-REceive (SCORE) may be used to generate a time-variant receive beam that follows the reflected echo traversing the ground. The paper details this concept by formulating a mathematical model from a physical perspective and relating it to the digital beam-forming algorithms. Several variants of the imaging mode and the effect on the SAR performance have been addressed, such as the pulse extension loss and the weight update rate. Last, the paper covers frequency-dependent (dispersive) beam-forming, which benefits from the angle-to-frequency mapping, due to the side-looking SAR geometry. Two digital hardware implementation variants of dispersive SCORE were shown and the respective mathematical models were presented.

SAR instruments utilizing single-beam (basic) SCORE are capable of imaging swath widths of a few tens of kilometers in stripmap mode. Ultra-wide swath imaging requires multiple SCORE antenna beams; this topic is covered in Part II of the tutorial trilogy, which also addresses multiple azimuth channels (MACs), digital data stream management, and aspects of proper feed array design. However, multi-SCORE ultra-wide swath SAR images are interrupted by gaps also known as blind ranges. The width of these gaps, which are a consequence of the transmit events, is analyzed providing expressions for the dependencies on the system parameters and the geometry. Part III deals with staggered SAR, a highly advanced technique, which allows removing the aforementioned image gaps. This is possible by changing the pulse repetition interval on a pulse-to-pulse basis according to a pre-determined sequence. As it turns out, this affects the SAR azimuth performance, requiring special mitigation techniques, which are explained in the last part of the trilogy.

[9]In the strict sense, the term FIR filter might not apply in the case of time-varying coefficients; we keep the terminology here, trusting that the readers understand what is meant.

References

[1] A. Moreira, P. Prats-Iraola, M. Younis, G. Krieger, I. Hajnsek, and K. Papathanassiou, "A tutorial on synthetic aperture radar," *IEEE Geoscience and Remote Sensing Magazine*, vol. 1, no. 1, pp. 6–43, Mar. 2013.

[2] F. Henderson and A. Lewis, *Manual of Remote Sensing: Principles and Applications of Imaging Radar*. New York: John Wiley & Sons, 1998.

[3] J. C. Curlander and R. N. McDonough, *Synthetic Aperture Radar: Systems and Signal Processing*. New York: John Wiley, 1991.

[4] C. Elachi and J. van Zyl, *Introduction to the Physics and Techniques of Remote Sensing*. New York: John Wiley & Sons, 2006.

[5] I. Woodhouse, *Introduction to Microwave Remote Sensing*. CRC, Taylor & Francis, 2006.

[6] I. G. Cumming and F. H. Wong, *Digital Processing of Synthetic Aperture Radar Data: Algorithms And Implementation*. Artech House, 2005.

[7] M. Younis, "Digital beam-forming for high resolution wide swath real and synthetic aperture radar," Ph.D. dissertation, Institut für Höchstfrequenztechnik und Elektronik, Universität Karlsruhe, July 2004.

[8] M. Younis, F. Bordoni, N. Gebert, and G. Krieger, "Smart multi-aperture radar techniques for spaceborne remote sensing," in *Proc. Int. Geoscience and Remote Sensing Symposium IGARSS'08*, Boston, MA, USA., July 2008.

[9] N. Gebert, "Multi-channel azimuth processing for high-resolution wide-swath SAR imaging," Ph.D. dissertation, German Aerospace Center (DLR), Aug. 2009.

[10] C. Fischer, C. Schaefer, and C. Heer, "Technology development for the HRWS (High Resolution Wide Swath) SAR," in *International Radar Symposium IRS'07*, Sept. 2007.

[11] G. D. Callaghan, "Wide-swath space-borne SAR: Overcoming the trade-off between swath-width and resolution," Ph.D. dissertation, University of Queensland's, 1999.

[12] M. Süß and W. Wiesbeck, "Side looking SAR system," U.S. Patent 6 870 500, Mar., 2005.

[13] M. Younis, P. López-Dekker, F. Bordoni, P. Laskowski, and G. Krieger, "Exploring the trade-space of MIMO SAR," in *Proc. Int. Geoscience and Remote Sensing Symposium IGARSS'13*, Melbourne, Australia, July 2013.

[14] M. Younis, P. López-Dekker, and G. Krieger, "MIMO SAR operation modes and techniques," in *Proc. European Conference on Synthetic Aperture Radar EUSAR'2014*, Berlin, Germany, June 2014.

[15] E. Fishler, A. Haimovich, R. Blum, L. cimini, D. Chizhik, and R. Valenzuela, "MIMO radar: An idea whose time has come," in *Proceedings of the IEEE Radar Conference*, Apr. 2004, pp. 71–78.

[16] G. Krieger, N. Gebert, and A. Moreira, "Multidimensional waveform encoding: A new digital beamforming technique for synthetic aperture radar remote sensing," *IEEE Transactions on Geoscience and Remote Sensing*, vol. 46, no. 1, pp. 31–46, Jan. 2008.

[17] A. Freeman, W. Johnson, B. Huneycutt, R. Jordan, S. Hensley, P. Siqueira, and J.Curlander, "The 'Myth' of the minimum SAR antenna area constraint," *IEEE Transactions on Geoscience and Remote Sensing*, vol. 38, no. 1, pp. 320–324, Jan. 2000.

[18] M. Younis, F. Q. de Almeida, P. López-Dekker, and G. Krieger, "Techniques and modes for multi-channel SAR instruments," in *Proc. European Conference on Synthetic Aperture Radar EUSAR'2016*, Hamburg, Germany, June 2016.

[19] N. Gebert, G. Krieger, and A. Moreira, "Digital beamforming on receive: Techniques and optimization strategies for high-resolution wide-swath SAR imaging," *IEEE Transactions on Aerospace and Electronic Systems*, vol. 45, pp. 564–592, 2009.

[20] W. Imbriale, S. Gao, and L. Boccia, Eds., *Space Antenna Handbook*. John Wiley & Sons, 2012.

[21] M. Younis, S. Huber, A. Patyuchenko, F. Bordoni, and G. Krieger, "Performance comparison of reflector- and planar-antenna based digital beam-forming SAR," *Int. Journal of Antennas and Propagation*, vol. 2009, June 2009. [Online]. Available: http://www.hindawi.com/journals/ijap/2009

[22] A. Moreira, G. Krieger, I. Hajnsek, K. Papathanassiou, M. Younis, P. López-Dekker, S. Huber, M. Villano, M. Pardini, M. Eineder, F. D. Zan, and A. Parizzi, "Tandem-L: A highly innovative bistatic SAR mission for global observation of dynamic processes on the earth's surface," *IEEE Geoscience and Remote Sensing Magazine*, vol. 3, no. 2, pp. 8–23, June 2015.

[23] S. Huber, M. Younis, G. Krieger, A. Patyuchenko, and A. Moreira, "Spaceborne reflector SAR systems with digital beamforming," *IEEE Transactions on Aerospace and Electronic Systems*, vol. 48, no. 4, pp. 3473–3493, Oct. 2012.

[24] P. Rosen, S. Hensley, S. Shaffer, W. Edelstein, Y. Kim, R. Kumar, T. Misra, R. Bhan, and R. Sagi, "The NASA-ISRO SAR (NISAR) mission dual-band radar instrument preliminary design," in *Proc. Int. Geoscience and Remote Sensing Symposium IGARSS'2017*, Fort Worth, USA, July 2017.
[25] M. Younis, C. Fischer, and W. Wiesbeck, "Digital beamforming in SAR systems," *IEEE Transactions on Geoscience and Remote Sensing*, vol. 41, no. 7, pp. 1735–1739, July 2003.
[26] M. Younis, P. López-Dekker, A. Patyuchenko, and G. Krieger, "Digital beamforming architecture and techniques for a spaceborne interferometric ka-band mission," in *Proceedings of the IEEE Radar Conference*, Ottawa, Canada, Apr. 2013.
[27] "Calibration and data reduction for digital beam forming instruments – technical reports," European Space Agency (ESA/ESTEC), Tech. Rep. ESA/ESTEC Contract Nr. 4000117363/16/NL/FE, Dec. 2018.
[28] M. Younis, C. Laux, N. Al-Kahachi, P. López-Dekker, G. Krieger, and A. Moreira, "Calibration of multi-channel spaceborne SAR – challenges and strategies," in *Proc. European Conference on Synthetic Aperture Radar EUSAR'2014*, Berlin, Germany, June 2014.
[29] S. Horst, J. Hoffman, D. Perkovic-Martin, S. Shaffer, T. Thrivikraman, P. Yates, and L. Veilleux, "Implementation of rf circuitry for real-time digital beam-forming sar calibration schemes," in *IET International Conference on Radar Systems (Radar 2012)*, Oct. 2012.
[30] M. Younis, A. Patyuchenko, S. Huber, G. Krieger, and A. Moreira, "A concept for a high performance reflector-based X-band SAR," in *Proc. European Conference on Synthetic Aperture Radar EUSAR'2010*, June 2010.
[31] C. A. Balanis, *Antenna Theory: Analysis and Design*, 4th ed. John Wiley & Sons, 2016.
[32] A. Patyuchenko, M. Younis, S. Huber, and G. Krieger, "Optimization aspects of the reflector antenna for the digital beam-forming SAR system," in *Proc. European Conference on Synthetic Aperture Radar EUSAR'2010*, June 2010.
[33] J. H. Blythe, "Radar systems," U.S. Patent 4 253 098, Feb., 1981.
[34] J. T. Kare, "Moving receive beam method and apparatus for synthetic aperture radar," U.S. Patent 6 175 326, Jan., 2001.
[35] M. Süß and W. Wiesbeck, "Side-looking synthetic aperture radar system," European Patent EP 1 241 487, Sept., 2002.
[36] A. Freeman, G. Krieger, P. Rosen, M. Younis, W. Johnson, S. Huber, R. Jordan, and A. Moreira, "SweepSAR: Beam-forming on receive using a reflector-phased array feed combination for spaceborne SAR," in *Proceedings IEEE Radar Conference (RadarCon'09)*, Pasadena, U.S.A., May 2009.
[37] M. Süß, B. Grafmüller, and R. Zahn, "A novel high resolution, wide swath SAR," in *Proceedings Int. Geoscience and Remote Sensing Symposium IGARSS'01*, vol. 3, Sydney, Australia, July 2001, pp. 1013–1015.
[38] M. Younis, F. Q. de Almeida, F. Bordoni, P. López-Dekker, and G. Krieger, "Digital beamforming techniques for multi-channel synthetic aperture radar," in *Proc. Int. Geoscience and Remote Sensing Symposium IGARSS'2016*, Beijing, China, July 2016.
[39] M. Younis, T. Rommel, F. Bordoni, G. Krieger, and A. Moreira, "On the pulse extension loss in digital beamforming SAR," *IEEE Geoscience and Remote Sensing Letters*, vol. 12, no. 7, pp. 1436–1440, July 2015.
[40] M. Younis, F. Q. de Almeida, S. Huber, M. Zonno, M. R. Cassola, S. Hensley, and G. Krieger, "The cost of opportunity for gapless imaging," in *Proc. Int. Geoscience and Remote Sensing Symposium IGARSS'19*, Yokohama, Japan, July 2019.
[41] S. R. Cloude, *Polarisation: Applications in Remote Sensing*. New York: Oxford Univ. Press, 2009.
[42] J.-S. Lee and E. Pottier, *Polarimetric Radar Imaging: From Basics to Applications*. CRC Press, 2009.
[43] M. Naranjo, A. Montesano, F. Monjas, M. Gomez, R. Manrique, F. Heliere, and K. van't Klooster, "Biomass P-band SAR reflector antenna - feed S/S breadboarding," in *Proc. European Conference on Synthetic Aperture Radar EUSAR'2014*, Berlin, Germany, June 2014.
[44] P. Valle, G. Orlando, R. Mizzoni, F. Hélière, and K. van't Klooster, "P-band feedarray for BIOMASS," in *Proc. European Conference on Antennas and Propagation EUCAP'2012*, Prague, Czech Republic, Mar. 2012, pp. 3426–3430.
[45] K. Raney, "Comparing compact and quadrature polarimetric SAR performance," *IEEE Geoscience and Remote Sensing Letters*, vol. 13, no. 6, pp. 861–864, June 2016.
[46] M. Villano, G. Krieger, U. Steinbrecher, and A. Moreira, "Simultaneous single-/dual- and quad-pol SAR imaging over swaths of different widths," *IEEE Transactions on Geoscience and Remote Sensing*, vol. 58, no. 3, pp. 2096–2103, Mar. 2020.
[47] F. Q. de Almeida, M. Younis, G. Krieger, S. Hensley, and A. Moreira, "Investigation into the weight update rate for scan-on-receive beamforming," in *Proc. IEEE Radar Conference*, Florence, Italy, Sept. 2020.
[48] H. Ghaemi, S. Shaffer, and S. Hensley, "Onboard digital beamforming: Algorithm and results," in *Proc. Int. Geoscience and Remote Sensing Symposium IGARSS'2014*, Quebec City, Canadaa, July 2014.
[49] S. Huber, "Spaceborne SAR systems with digital beamforming and reflector antenna," Ph.D. dissertation, Deutsches Zentrum für Luft- und Raumfahrt: Forschungsbericht, Sept. 2014.
[50] M. Younis, "NESZ-formulation for planar multi-channel SAR," German Aerospace Center, Microwaves and Radar Institute, Technical Note HR-RK-TN MY101, issue 2.3, Apr. 2019.